Key Points:
- A parameterization for representing unresolved rocket dust storms in Martian GCM is proposed and employed in simulations with the LMD model
- GCM simulations featuring the rocket dust storm parameterization reproduce the detached dust layers observed by MCS during the dusty seasons
- The formation of detached dust layers within Mars clear seasons L_s after 270° in MY29 is underestimated in the simulations compared to the observations

Supporting Information:
- Supporting Information S1

Parameterization of Rocket Dust Storms on Mars in the LMD Martian GCM: Modeling Details and Validation

Chao Wang[1,2,3] (ID), **François Forget**[1] (ID), **Tanguy Bertrand**[1] (ID), **Aymeric Spiga**[1] (ID), **Ehouarn Millour**[1] (ID), **and Thomas Navarro**[1] (ID)

[1]Laboratoire de Météorologie Dynamique/IPSL, Sorbonne Université, École Normale Supérieure, PSL Research University, École Polytechnique, CNRS, Paris, France, [2]School of Geographic Sciences, East China Normal University, Shanghai, China, [3]Shanghai Institute of Meteorological Science, Shanghai, China

Abstract The origin of the detached dust layers observed by the Mars Climate Sounder aboard the Mars Reconnaissance Orbiter is still debated. Spiga et al. (2013, https://doi.org/10.1002/jgre.20046) revealed that deep mesoscale convective "rocket dust storms" are likely to play an important role in forming these dust layers. To investigate how the detached dust layers are generated by this mesoscale phenomenon and subsequently evolve at larger scales, a parameterization of rocket dust storms to represent the mesoscale dust convection is designed and included into the Laboratoire de Météorologie Dynamique (LMD) Martian Global Climate Model (GCM). The new parameterization allows dust particles in the GCM to be transported to higher altitudes than in traditional GCMs. Combined with the horizontal transport by large-scale winds, the dust particles spread out and form detached dust layers. During the Martian dusty seasons, the LMD GCM with the new parameterization is able to form detached dust layers. The formation, evolution, and decay of the simulated dust layers are largely in agreement with the Mars Climate Sounder observations. This suggests that mesoscale rocket dust storms are among the key factors to explain the observed detached dust layers on Mars. However, the detached dust layers remain absent in the GCM during the clear seasons, even with the new parameterization. This implies that other relevant atmospheric processes, operating when no dust storms are occurring, are needed to explain the Martian detached dust layers. More observations of local dust storms could improve the ad hoc aspects of this parameterization, such as the trigger and timing of dust injection.

Plain Language Summary On Mars, dust is of major importance to the Martian atmosphere, analogous to the importance of water to the Earth's atmosphere. But unlike the water on Earth, the distribution of dust on Mars is still not well understood, particularly the vertical distribution. The Mars Climate Sounder aboard the Mars Reconnaissance Orbiter found that the dust on Mars is detached at ~20–40 km in altitude in the Martian atmosphere, rather than concentrated in the near-surface atmosphere and decreasing as the pressure decreases, as scientists have thought since the 1980s. The reason for the detached dust layers is still debated. In this paper, we implemented a modeling study by simulating the small-scale deep rocket dust storm in a Global Climate Model to explore the origins of the detached dust layers. We found that when the Global Climate Model included rocket dust storms, the simulations produced the detached structures of dust on Mars. This suggests that the rocket dust storm is responsible for the formation of the detached dust layers. Meanwhile, the rocket dust storms cannot reproduce all the detached dust layers observed by Mars Climate Sounder. This implies that some unknown atmospheric processes can also contribute to the existence of the detached dust layers.

1. Introduction

Airborne dust is a crucial component of the Martian climate system. It affects the Martian atmosphere's radiative balance by absorbing and scattering shortwave solar radiation, as well as absorbing and emitting longwave infrared radiation. It has a strong impact on Martian meteorology and climate.

The vertical distribution of dust constrains our understanding of the Martian dust cycle. For a long time, taking into consideration the combined effects of gravitational sedimentation and vertical mixing, dust has been assumed to be well mixed in the lower atmosphere up to a level in the troposphere and to decrease

as a function of pressure above this level (Conrath, 1975; Forget et al., 1999). However, this assumption is challenged by the observations of the Mars Climate Sounder (MCS) instrument aboard the Mars Reconnaissance Orbiter (MRO; McCleese et al., 2007). MCS demonstrated the year-round existence of detached dust layers in the middle troposphere of Mars. These detached dust layers are characterized by mass mixing ratio maxima at 15–25 km (~60–120 Pa on Mars), which is above the planetary boundary layer (PBL), during Martian clear seasons (northern spring and summer). The dust concentration in these maxima can be 2–10 times larger than the concentration near the surface (Heavens et al., 2011a, 2011b; Heavens et al., 2011; McCleese et al., 2010). During Martian dusty seasons (northern autumn and winter), the detached dust layers appear to have higher altitudes and concentrations. Meanwhile, their altitudes and concentrations also vary significantly in these seasons (see Figures 10 and 11 in McCleese et al., 2007). The detached dust layers observed by MCS are mainly distributed over tropical latitudes, with high detached layers over the poles in the summer hemisphere. The longitudinal variability of the detached dust layers is relatively weak (Heavens et al., 2014). This detached dust layer phenomenon has been confirmed directly by limb observations using the Thermal Emission Spectrometer on Mars Global Surveyor (Guzewich et al., 2013) and the Compact Reconnaissance Imaging Spectrometer for Mars onboard MRO (Smith et al., 2013) and possibly by radio occultation with the Spectroscopy for the Investigation of Characteristics of the Atmosphere of Mars instrument on Mars Express (Määttänen et al., 2013). The detached dust layers have also been indirectly identified by their thermal signature in MCS data (Navarro, Forget, et al., 2014).

The origin of the detached dust layer phenomenon remains uncertain.

Dust storms, which occur on local-, regional-, and planet-encircling scales, are regularly observed on Mars, with the largest storms occurring from southern spring to summer (often termed the "dust storm season"; Cantor, 2007; Cantor et al., 2001; Wang & Richardson, 2015). Many types of regional and larger storms, resulting from lifting over large areas, have been numerically modeled in traditional Global Climate Models (GCMs; Basu et al., 2004, 2006; Kahre et al., 2006; Mulholland et al., 2013, 2015; Newman & Richardson, 2015; Newman et al., 2002). In some of these simulations, dust with detached structures are simulated, for instance, as shown in Newman et al. (2002). However, compared to the MCS-observed detached dust layers, the resulting dust layers in their studies are, first, not as opaque as the MCS-observed ones (Heavens et al., 2011a). Second, the elevated dust layers usually last for few sols in the Laboratoire de Météorologie Dynamique (LMD) Mars GCM. They are short lived compared to those in the MCS observations, which can remain for months or year-round, even outside the dust storm seasons. No other Mars GCM has been shown to produce elevated dust layers that match those observed by MCS in terms of their life length. Moreover, the detached dust layers are observed in the tropics during most of northern spring and summer by MCS (Heavens et al., 2011a), yet large dust storms are rarely observed during this period (Cantor et al., 2001).

What can explain the observed departure from a vertically well-mixed atmosphere? Several mechanisms have been proposed.

First, small-scale dust devils are suspected to be the dominant phenomena maintaining the atmospheric dust loading during the northern spring and summer (Kahre et al., 2006). Heavens et al. (2011a) evaluated their capacity to lift dust particles into the high atmosphere, and the results suggested that dust devils cannot create detached dust layers as high as observed. The observed altitudes of dust devils are not higher than ~8 km (Fisher et al., 2005), which is much lower than the typical altitude of MCS-observed detached dust layers.

Second, scavenging of dust by water ice particles could also explain the formation of the detached dust layers (Heavens et al., 2011a). In water ice clouds, ice crystals grow onto dust particles (heterogeneous nucleation). The increase of a dust particle's mass enhances its sedimentation velocity. When the particles sediment to a level where the temperature is higher than the condensation temperature, ice sublimes and dust concentration below the ice cloud are enriched, hence forming a detached dust layer. This scavenging process has been elaborately parameterized in the Martian GCM developed at the LMD (Navarro, Madeleine, et al., 2014). It was found that dust scavenging by water ice alone fails to reproduce the detached dust layers observed by MCS.

Overall, so far, all endeavors to model dust lifting in a traditional GCM fail to reproduce the MCS-observed detached dust layers. The radiative heating of the dust does not create detached layers except for the case of the "solar escalator" (Daerden et al., 2015). The detached dust layers observed by the light detection and ranging instrument on the Phoenix Lander were simulated with the Global Environmental Multiscale

model for Mars by Daerden et al. (2015). In their simulation, the surface dust is lifted into the atmosphere due to large wind shear. The heating of the dust by solar radiation then causes buoyant instability and mixing across the top of the PBL. In the following sols (one sol means one Martian day), solar heating of the dust causes it to "escalate" slowly, leading to a detached dust layer remaining in the troposphere. This study highlights the fact that solar heated dust layers tend to be lifted and could create detached layers on Mars. However, in most cases when modeled at GCM scales, it seems that in general this process cannot create all the detached dust layers observed on Mars.

In contrast with coarse-resolution GCMs, however, dust clouds are subjected to strong vertical convective motion in fine-resolution mesoscale models. Two processes detailed below have been explored to simulate dust vertical motion in Martian mesoscale models, that is, slope winds (Rafkin et al., 2002) and "rocket dust storms" (Spiga et al., 2013). In both cases, dust layers, resembling the MCS-like detached dust layers, could be produced.

The thermally driven slope winds on Mars can be 2.5 times stronger than those on Earth under similar conditions (Spiga, 2011; Ye et al., 1990). The daytime upslope flow blows dust from the bottom to the top of a mountain, continues to raise up above the mountain top, and diverges horizontally at high altitudes. Thus, an orographic circulation is produced. This specific circulation around the volcano Arsia Mons was simulated by Rafkin et al. (2002) with the Mars Regional Atmospheric Modeling System. In their simulation, a "spiral dust cloud" formed at an altitude of ∼20 km, which implies that the dust lifted and transported by slope winds is capable of penetrating beyond the PBL and forming a detached dust layer. The altitude of the spiral cloud resembled that of the observed detached dust layers. In addition, by investigating the MCS-observed extreme detached dust layers outside of regional and global dust storms over Olympus Mons and the Tharsis Montes, Heavens et al. (2015) explored how the MCS observations are connected to the mesoscale orographic circulation. Heavens et al. (2015) also found that the vertical mixing caused by the orographic circulation could be even stronger than Rafkin et al.'s (2002) simulation.

A rocket dust storm, using terminology originally proposed by Spiga et al. (2013), is a storm that can raise dust particles rapidly and efficiently to high altitudes in the Martian troposphere (30–50 km). Spiga et al. (2013) showed that, after lifting and during daytime, the evolution of any low-level local dust storm of sufficiently high opacity will be governed by deep mesoscale convective motions driven by dust solar heating. Combined with the strong large-scale horizontal winds, the dust particles, lifted to high altitudes, are then spread horizontally to form a detached dust layer. Due to the nocturnal sedimentation of dust, which is less efficient compared to the daytime deep convection, and due to the further radiatively induced convection that occurs on the following sol, the detached dust layer remains stable for several Martian sols. A rocket dust storm can therefore be a plausible origin of detached dust layers. However, it is not possible for a GCM to directly represent this process because the rocket dust storm motions occur at scales that are finer than a traditional GCM's horizontal resolution. As Spiga et al. (2013) pointed out, to further explore the origins of the MCS-observed detached dust layers as well as the interactions between dust and other atmospheric components, it is necessary to parameterize the mesoscale deep convection, which is a robust process missing in any Martian GCM. Such a parameterization is also necessary to investigate the global and seasonal variabilities of the detached dust layers on Mars, which is too time intensive to perform with mesoscale models.

In this paper, our objective is to parameterize the rocket dust storms in a Martian GCM to explore the role of mesoscale dust convection in forming the detached dust layers on Mars. To do so, a new subgrid parameterization for rocket dust storms to represent the mesoscale dust convection is designed and implemented in the LMD Martian GCM and tested in simulations in which dust injection from the surface is simply assumed when the dust opacity is measured to significantly increase in the available observed dust climatology. A brief general description of the LMD Martian GCM can be found in section 2. The parameterization is detailed in section 3. In section 4, results and sensitivity studies are presented. The simulated dust vertical structures are then compared to the MCS observations (section 5). In section 6, we state the conclusions of this study.

2. The LMD Martian GCM

The LMD Martian GCM was originally developed in the early 1990s. It is composed of a grid point dynamic core, integrating the hydrodynamic equations with a finite difference method and a comprehensive set

of physical packages taking into account the radiative transfer (Forget et al., 1999), the dust cycle (Madeleine et al., 2011), the water cycle (Madeleine et al., 2012; Montmessin et al., 2004; Navarro, Madeleine, et al., 2014), PBL mixing (Colaïtis et al., 2013), and other physical processes (see details in Forget et al., 1999, 2011).

On Mars, the main radiative agents are gaseous CO_2 and aerosols, that is, airborne dust and water ice. For CO_2, a wideband model is adopted in the GCM to accurately simulate the emission and absorption of radiation in the 15-μm bands (Hourdin, 1992). The Doppler effect, the broadening of CO_2 molecular lines at low pressure, and nonlocal thermal equilibrium are also included. In the near-infrared bands of CO_2, atmospheric heating due to the absorption of solar radiation is parameterized (Forget et al., 1999). The radiative effect of dust particles is included in the radiative transfer equations, particularly the multiple scattering by dust particles outside the CO_2 15-μm bands. The radiative properties of dust particles from Wolff et al. (2006, 2009) are used as the most accurate dust scattering properties published to date.

Dust is described in the GCM by using a semiinteractive scheme (Madeleine et al., 2011). It is constantly injected from the surface at all times and all places. The shape of the vertical profile of dust is free to evolve through transport, mixing, and sedimentation, but the total column dust optical depth (CDOD) in the GCM is rescaled to a daily observation-based CDOD map (also called prescribed dust scenario; Montabone et al., 2015). This transport scheme allows a better representation of the dust distribution. The transport of dust is represented by a two-moment scheme (Madeleine et al., 2011). The two moments are, respectively, the mass mixing ratio and the number mixing ratio. The advection of each moment is performed separately. By assuming a lognormal size distribution, the effective radius of dust particles can be computed. The optical properties of the dust, such as opacity, extinction coefficient, and optical depth, can thus be obtained.

3. Modeling Strategy for the Rocket Dust Storm Parameterization

The objective of this parameterization is to represent the mesoscale dust convection inducing rocket dust storms in the GCM, so that the dust will not only mix in the lower part of the troposphere (as assumed before) but also get injected up to high altitudes as predicted in mesoscale models. Owing to convective motions, the main difficulty in this parameterization, as explained above, is that the rocket dust storm happens at scales smaller than the GCM's horizontal resolution, which is typically ~250 km. In order to better represent the real size of the rocket dust storm, subgrid-scale convective motion induced by radiative heating of dust must be represented.

In practice, we assume that a fraction of a horizontal grid cell is occupied by the local storm, and the rest only contains the usual environment dust present before the local dust storm event occurs. Two distinct dust tracers (transported by resolved motions in the GCM) are thus used in the rocket dust storm parameterization, that is, the "environment dust" and the "storm dust." The results from mesoscale simulations of the rocket dust storm (Spiga et al., 2013) are used to calibrate this parameterization.

3.1. Trigger Assumption

As mentioned before, the CDOD in the GCM is driven by a prescribed dust scenario derived from observations. In the parameterization, the onset of a dust storm is thus implemented in a grid cell when a sufficiently large CDOD increase ($\Delta\tau_{dust}$) is detected. When $\Delta\tau_{dust}$ in one GCM grid cell between one sol and the next is greater than 0.2, we assume that a significant dust storm occurred and that strong mesoscale deep convection would have occurred also; thus, the parameterization should be triggered. This strategy is based on the assumption that the dust particles lifted by a rocket dust storm will result in a rapid and large increase of dust optical depth. By setting this criterion ($\Delta\tau_{dust} > 0.2$), we found that the set of dust storms triggered by the GCM is comparable to the observed ones from Cantor et al. (2006; see Figure 1). In particular, some storms are obtained around the polar caps in northern summers and winters. In the equatorial regions, several storms are obtained during the dusty seasons, while almost no storm is obtained during the clear seasons. The criterion is also helpful to improve computational efficiency. Below this criterion, injecting a smaller amount of dust produces a weak response which is negligible in the GCM. In this study, the trigger of the dust storms, which are observed by satellites, is different from the mechanisms based on the local meteorological conditions, such as near-surface wind stress or energy available to drive convective vortices. However, there are differences in the locations and frequencies of the identified dust storms from GCM dust scenarios and Cantor et al.'s (2006) study. Such as, in the dusty season of MY27, more dust events are identified in the dust scenario than those in Cantor et al.'s (2006) study. The possible cause may be that, from Figure 21 in Montabone et al. (2015), three dusty periods
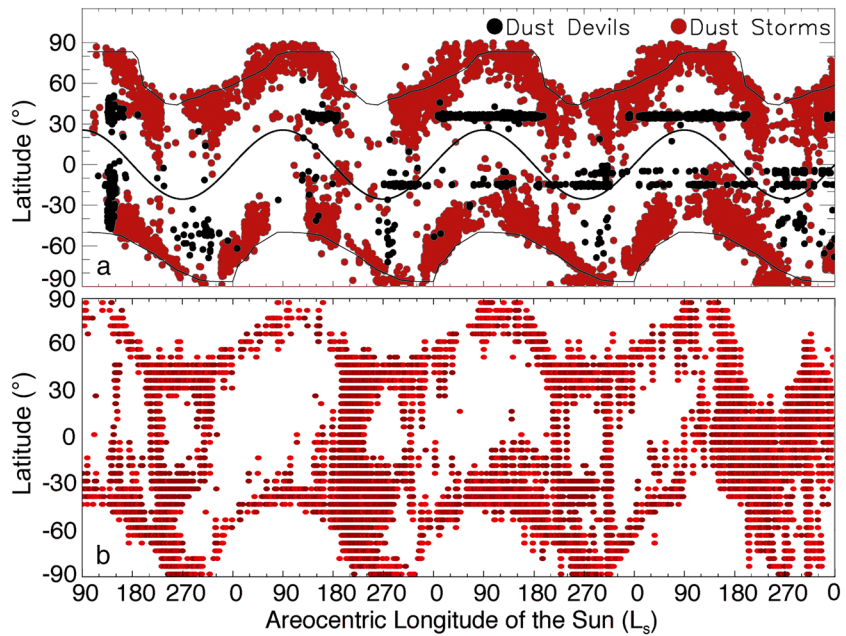
Figure 1. (a) Latitudinal distribution of Martian dust devils and storms versus areocentric longitude of the Sun, from MY24 to MY27 (adapted from Cantor et al., 2006). (b) Dust storms identified from the prescribed dust scenarios (Montabone et al., 2015) where column dust optical depth changes larger than 0.2 per sol are observed during the same time period. Note that the cluster of dust storms in MY25 is associated with the global dust storm.

are found in MY27, around L_s 150°, 230°, and 320°. But from MY24 to MY26, there are only one or two dusty periods. Thus, dust optical depth varies more in MY27 than in the other three Martian years, which results in more dust events in the GCM. The discrepancy may also hint that the threshold of $\Delta\tau_{dust}$ is not uniform at all places and times. It could be location dependent and/or season dependent. The differences could also result from some of the dust storms identified by Cantor et al. (2006) not being rocket dust storms (i.e., by some storms having $\Delta\tau_{dust} \leq 0.2$ per sol). Additionally, when large-scale dust storms (with $\Delta\tau_{dust} > 0.2$) occur, they are treated as an ensemble of adjacent rocket dust storms.

3.2. Dust Injection

During the daytime, the amount of dust lifted by the storm is directly associated with radiative warming in the rocket dust storm. The dust optical depth in each layer of pressure thickness dp is given by

$$d\tau_{dust} = \frac{3}{4} \frac{Q_{ext,\lambda}\, q}{\rho_{dust}\, r_{eff}\, g}\, dp \tag{1}$$

where $Q_{ext,\lambda}$ is the dust extinction coefficient at a given wavelength λ, q is the mass mixing ratio of the dust (kg/kg), ρ_{dust} is the density of the dust particle (2,500 kg/m^3), r_{eff} is the effective radius of the dust particle, and g is the Martian gravitational acceleration. For a given sol-to-sol increase $\Delta\tau_{dust}$, the flux of lifted dust v_{lift} (kg·m^{-2}·s^{-1}) can be estimated by

$$v_{lift} = \frac{4}{3} \frac{\Delta\tau_{dust}\, \rho_{dust}\, r_{eff}}{\Delta t\, Q_{ext,\lambda}} \tag{2}$$

with Δt the duration of the lifting per sol (s).

The dust injection from the surface into the atmosphere is only performed in the morning, from Martian local time (LT) 10:00 (t_{start}) to 12:00 (t_{end}) (in equation (2), $\Delta t = (t_{end} - t_{start}) * 88775/24$). t_{start} and t_{end} are chosen empirically. A good match among GCM simulations, mesoscale simulations, and observations is reached by activating dust lifting in this local time range (see text in section 4.2.3). The goals of the match have two aspects. First, for each individual rocket dust storm, the vertical convection (such as the magnitude of the vertical velocity and the altitude reached) of the storm should behave similarly to those in the mesoscale studies. Second, the annual simulated vertical dust distribution should be as close as possible to the MCS observations, that is, the formation of the detached dust layers and the variation/evolution of the altitudes of the detached dust layers over the simulated Martian year.

After the onset of the dust storm, an estimation of the fractional area occupied by the local dust storm within the GCM grid cell is needed. The maximum optical depth of the OMEGA local dust storm studied by Määttänen et al. (2009) and Spiga et al. (2013) is ∼10, extending over one scale height above the surface (i.e., $\Delta p \approx 200$ Pa). By assuming an extinction coefficient of 2.4, effective radius of 2 μm, and dust particle density of 2,500 kg/m^3, a corresponding reference mass mixing ratio can be computed through

$$q_{ref} = \frac{4}{3} \frac{\rho_{dust} \, r_{eff} \, g}{Q_{ext,\lambda} \, \Delta p} \, \tau \qquad (3)$$

which gives $q_{ref} = 5 \times 10^{-4}$ kg/kg. By comparing the mass mixing ratio of the lifted storm dust spread over the entire grid cell to this reference value, that is, assuming the optical depth for all the local dust storms is 10, the areal fraction of the GCM grid occupied by the local storm can be estimated. If the mass mixing ratio of the grid is larger than or equal to q_{ref}, the fraction is set equal to 1.

For the sake of comparison between model outputs and existing diagnostics of MCS dust observations, the density-scaled opacity (DSO) is employed to describe dust distributions. It can be written as

$$\frac{d\tau_{dust}}{\rho} = \frac{3}{4} \frac{Q_{ext,\lambda}}{\rho_{dust} \, r_{eff}} q \qquad (4)$$

where ρ is the air density. This quantity is proportional to the dust mass mixing ratio and the aerosol heating rates (Heavens et al., 2010; Spiga et al., 2013).

3.3. Radiative Transfer

After the onset of a rocket dust storm, at each time step, the radiative transfer calculations are performed twice in a row. The first radiative transfer iteration is calculated with only environment dust. This gives the environmental heating rate $(\frac{dT}{dt})_{env}$ (where T is temperature) outside the dust storm. The second radiative transfer iteration features both the environment dust and the storm dust, which gives the heating rate $(\frac{dT}{dt})_{storm+env}$ inside the dust storm. The radiative effect due to the presence of the rocket dust storm (named "extra heating," $\Delta \mathcal{H}$) can be obtained by:

$$\Delta \mathcal{H} = \left(\frac{\partial T}{\partial t}\right)_{storm+env} - \left(\frac{\partial T}{\partial t}\right)_{env} \qquad (5)$$

3.4. Vertical Transport

Spiga et al. (2013) demonstrated through mesoscale modeling that the ascent of a rocket dust storm is controlled by the competing radiative warming and adiabatic cooling. In the parameterization we therefore assume that the extra heating $\Delta \mathcal{H}$ due to the presence of the storm dust is completely balanced by adiabatic cooling through vertical motion. From the Eulerian point of view, potential temperature for each layer in the GCM is modified by the adiabatic process, which is

$$\frac{\partial \theta}{\partial t} = \Delta \mathcal{H} \, \Pi^{-1} - w \frac{d\theta}{dz} \qquad (6)$$

where w is the vertical velocity inside the storm, z is altitude, θ is the potential temperature of air, and Π is the Exner function

$$\Pi = \left(\frac{P}{P_0}\right)^{\frac{R}{c_p}} \qquad (7)$$

where P is the pressure, P_0 is the reference pressure, R is the gas constant, and c_p is the specific heat capacity. By considering that the radiative warming is balanced by the vertical motion,

$$\frac{\partial \theta}{\partial t} = 0 \qquad (8)$$

Assuming the condition of hydrostatic equilibrium, the vertical velocity w can be written as

$$w = \frac{\Delta \mathcal{H}}{\frac{dT}{dz} + \frac{g}{c_p}} \qquad (9)$$

This equation leads to a comparable magnitude of vertical velocity in the GCM to the one simulated in the mesoscale models (Rafkin, 2009, 2012; Spiga et al., 2013). The values of the vertical velocities within the rocket
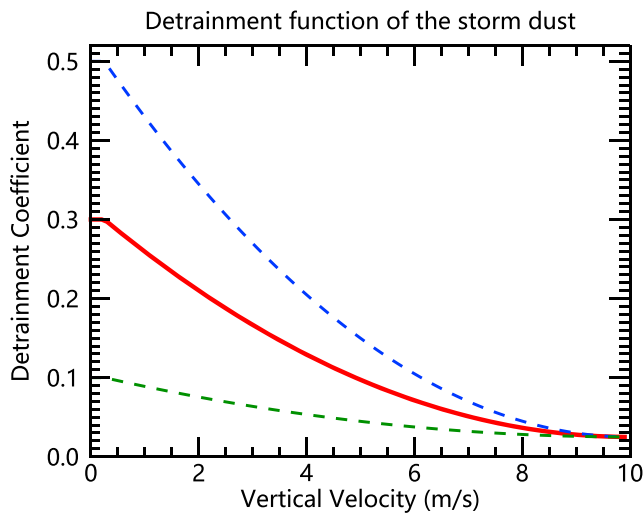
Figure 2. A quadratic function is used to describe the detrainment of the storm dust to the environment dust (see text). The coefficient of detrainment depends on the vertical velocity of the air parcel. The stronger the wind, the weaker the detrainment. In the best-guess parameterization, the maximum and minimum of detrainment coefficient are set to 30% and 2.5%, respectively (red line). The detrainment functions in the sensitivity studies for cases weak detrainment (green dashed line; see the definitions of cases in Table 1) and strong detrainment (blue dashed line) are also shown. The maxima of detrainment for case weak detrainment and strong detrainment are 10% and 50%, respectively.

dust storm are about 2 orders of magnitude larger than the typical vertical velocities in GCM simulations (∼0.1 m/s).

After estimation of the vertical velocity, in the subgrid region where the rocket dust storm begins, the storm dust tracer is vertically advected in the parameterization by a Van Leer transport scheme (Hourdin & Armengaud, 1999; Van Leer, 1977). The environmental dust is not involved in this vertical convection. Note that, after the vertical transport, an average of the storm dust and environment dust over the whole grid cell is used for other GCM computations (e.g., vertical diffusion and sedimentation) that require knowledge of dust abundance in that grid cell. For each time step during the simulation, the storm dust is also transported by large-scale motions in the GCM, such as the Hadley cell, which is typically strengthened due to the enrichment of dust.

3.5. Detrainment of Storm Dust

Once transferred to high altitude, if the velocity of the storm dust decreases, the storm dust starts to detrain into environment dust. This process represents the effects of dilution and mixing of the storm dust and how dust injected into the atmosphere by dust storms replenishes the ambient veil of dust particles on Mars. The detrainment of storm dust is a key process in this parameterization, because it controls the amount of storm dust remaining in the convective storm, thus the radiative heating rate $\Delta \mathcal{H}$ imposed by this storm. It is worth noting that when the convection of the triggered dust storm is not deep enough, it is possible that the dust storm will dissipate before penetrating the PBL. Mixing process (i.e., entrainment and detrainment) in cumulus convection on Earth has been parameterized by various methods (de Rooy et al., 2013). For deep convection, Large Eddy Simulations show that variations of mass flux are determined by detrainment rather than entrainment (Böing et al., 2012; de Rooy & Siebesma, 2010). An analytical expression for detrainment, in terms of buoyancy, vertical velocity, and cloud fraction, is given by de Rooy & Siebesma (2010; see equation (28) in their study) for terrestrial cumulus convection. But unlike the Earth case, there are few studies exploring the fine-scale entrainment/detrainment on Mars. In this study, during the ascent of a storm, the effect of the buoyancy (alternatively, the extra heating) and the fraction of the local storm can be represented by the vertical velocity to some extent (see equation (9)). Combined with the fact that a deeper dust layer will form given a smaller detrainment rate, for the sake of simplicity, a function is defined by assuming that the coefficient of detrainment is inversely dependent on the vertical velocity of the storm dust (shown in Figure 2), that is, the lower the velocity of the storm dust, the more efficient the detrainment.

3.6. Horizontal Transportation and Sedimentation

The motion of the storm is also controlled by the large-scale horizontal winds from the dynamics of the GCM. It becomes particularly obvious after the rocket dust storm penetrates beyond the PBL.

During the nighttime, the storm dust loses its convective energy (solar energy). It sediments for two reasons. The first is gravity. According to Stokes's law, the terminal velocity of dust is proportional to the effective radius of the particle. In a rocket dust storm, it is modeled that the effective radius of the dust particles is larger than that of the environment dust because of the strong vertical wind associated with the rocket dust storm. The sedimentation for storm dust will therefore be more efficient than for environment dust. The second reason is that the dusty air parcel (dust storm) radiates more energy in the infrared bands than its environment, which results in a negative $\Delta \mathcal{H}$ during the night. Based on equations (5) and (9), which are applied at all times in the GCM, the velocities of the dust particles in the storm become negative (i.e., downward). This supports the downward motion of the storm dust in the nighttime.

4. Results

In this study, all the GCM simulations were performed at a spatial resolution of 64 × 48 grid cells in longitude and latitude and 29 vertical layers reaching a maximum altitude of ∼80 km. The CDOD in the model

Table 1
Key Parameter Values Used in the Sensitivity Studies

Name	Maximum of the detrainment	q_{ref}	t_{start}	t_{end}
BG (best-guess run)	0.3	5×10^{-4}	10:00	12:00
WD (weak detrainment)	0.1	5×10^{-4}	10:00	12:00
SD (strong detrainment)	0.5	5×10^{-4}	10:00	12:00
CS (clear storm)	0.3	2.5×10^{-4}	10:00	12:00
DS (dusty storm)	0.3	7.5×10^{-4}	10:00	12:00
EI (early injection)	0.3	5×10^{-4}	8:00	10:00
LI (late injection)	0.3	5×10^{-4}	12:00	14:00
LoI (long injection)	0.3	5×10^{-4}	10:00	14:00
SI (short injection)	0.3	5×10^{-4}	10:00	11:00

follows the prescribed "Martian Year 29" (MY29 hereafter) dust scenario. The water cycle and photochemistry are turned off during the simulation in order to better diagnose the performance of the parameterization. Several parameters (see Table 1) in the parameterization needed to simulate rocket dust storms in the GCM are unconstrained and difficult to estimate. These include (1) the efficiency of the detrainment, (2) the reference mass mixing ratio used to estimate the size of the subgrid-scale rocket dust storm, and (3) the starting time and duration of dust injection.

4.1. Best-Guess Run

After exploring parameter space, we found the best match to mesoscale simulations of individual storms and overall vertical dust distributions observed by MCS were given by using the "best-guess" parameters listed in Table 1. A simulation (best-guess (BG) case) with these parameters is performed. Figure 3 displays the evolution of the storm case BG, occurring at longitude 84.5°W, latitude 56.25°N, around $L_s = 153.8°$ in MY29, and the resulting detached dust layer. Before the onset of the rocket dust storm, no detached dust layers can be identified (Figure 3a). From LT 10:00 to 12:00, a rocket dust storm is triggered in the parameterization because the CDOD increases by ∼0.4 ($\Delta \tau_{dust}$). After the dust particles are lifted from the surface to the atmosphere, around LT 15:00 (Figure 3b), the rocket dust storm penetrates beyond the PBL, reaching an altitude of ∼18 km. Afterward, the dusty air parcel (rocket dust storm) keeps rising until the disappearance of solar heating. At ∼LT 20:00 (Figure 3c), the rocket dust storm reaches its highest altitude, ∼36 km. Not all of the storm dust is transferred to this altitude, because dust particles (storm dust) with low velocities are detrained to the environment dust as designed in the parameterization. After sunset, the storm dust sediments downward owing to gravity and the negative buoyancy induced by the dust infrared cooling. At LT 03:00 on the next sol, the detached dust layer is still present at ∼30 km, as shown in Figure 3d. Because the detached dust layer moves equatorward, Figure 3d displays values at 52.5°N (not 56.25°N as in Figures 3a–3c).

In this simulation, the detached dust layer peaks at ∼36 km. It is higher than the typical altitude that MCS observed, that is, 20–25 km as introduced in section 1. This is reasonable for two reasons: first, for an individual dust storm, the altitude it reached depends on its strength of convection. In this parameterization, a storm with higher $\Delta \tau_{dust}$ is expected to trigger deeper convection, and thus, it can reach a higher altitude. Therefore, the altitude an individual rocket dust storm reached is not necessarily restricted to the range of the typical altitude of MCS-observed detached dust layers. Second, MCS observes Mars at two operating local times, that is, 3:00 and 15:00. It is highly possible that MCS missed the moment when dust reached its highest altitude. In this case, the storm reached ∼36 km at 20:00 local time but had descended by ∼6 km by 3:00.

4.2. Sensitivity Experiments

In order to determine the sensitivities of the parameters listed in Table 1, eight simulations with different values were performed. q_{ref} is related to the property of the initial rocket dust storm. t_{start} and t_{end} are relevant to the lifting of dust particles. The detrainment function is associated with the interchange of storm dust and environment dust. Figures 4 and 5 summarize the evolutions of the rocket dust storm in the different simulations.

4.2.1. Detrainment

Among the parameters listed in Table 1, detrainment plays the most significant role in governing the evolution of the rocket dust storm. The functions of detrainment for the weak detrainment (WD) and strong detrainment
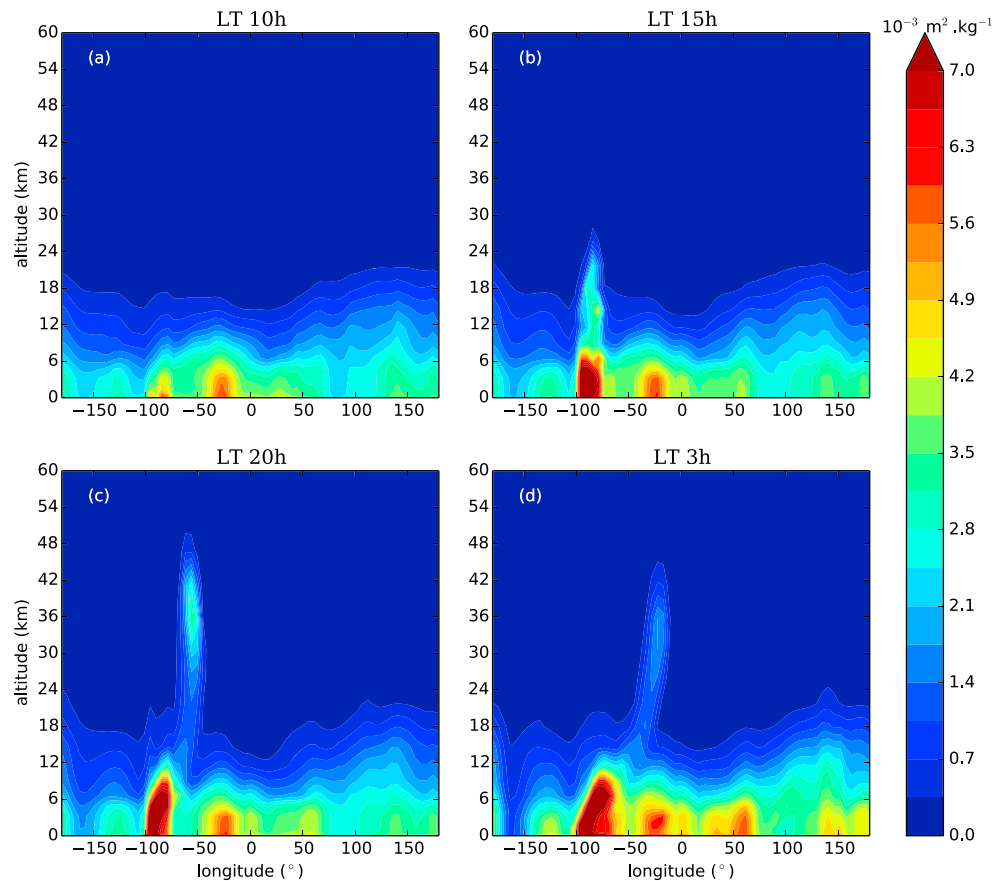
Figure 3. The best-guess case (Table 1) of a rocket dust storm. Cross sections of the dust visible density-scaled opacity at latitude = 56.25°N in (a) local time (LT) 10:00, (b) LT 15:00, and (c) LT 20:00 are shown. In (d), density-scaled opacity at latitude = 52.5°N and LT 03:00 (on the next sol) is shown. Season is late northern summer (L_s = 153.8–154.4°).

(SD) cases can be found in Figure 2. The top of Figure 4 shows the same results as in Figure 3 (for case BG) but for WD and SD. As expected, the simulation with the weakest detrainment exhibits the deepest dust convection. The energy for supplying this motion is provided by the extra heating from the absorption of solar energy by the storm dust, controlled by the contrast of the amount of the dust in the environment and in the storm. The larger the contrast, the larger the extra heating (see equation (5)). With a strong detrainment, the storm dust is more efficiently supplied to the environment dust. For a weak detrainment, a larger $\Delta \mathcal{H}$ is expected and hence the rocket dust storm is capable of advecting to a higher altitude, as occurs for case WD in Figure 4. In the strong detrainment case (case SD), the rocket dust storm blows the dust particles up to ~20 km in altitude, but no apparent detached dust layer forms. While in the WD case, the storm reaches ~42 km in altitude at LT 20:00 and remains at ~40 km by LT 03:00 the following sol. The altitude of the detached layer is higher by ~6 km than in the best-guess simulation.

4.2.2. Strength of the Initial Storm

Because of the lack of information on each individual dust storm's spatial size, a reference mass mixing ratio needs to be assumed (see text in section 3.2). This value represents the dustiness of the rocket dust storm. A clearer (case clear storm [CS]) or dustier (case dusty storm [DS]) storm will impact the estimation of the fraction of the storm. As a consequence, the contrast between the dust concentration of the environment and the storm will be changed. Varying the reference dust mass mixing ratio produces results similar to those produced by varying the detrainment strength by the same fractional amount but with less variations in altitude and dustiness of the simulated dust layers. In the best-guess simulation, the storm extends to ~36 km at LT 20:00. In case CS (Figure 4c3), a detached layer forms at ~20 km. While by contrast, the dustier storm rises higher than 40 km at LT 20:00 in case DS.
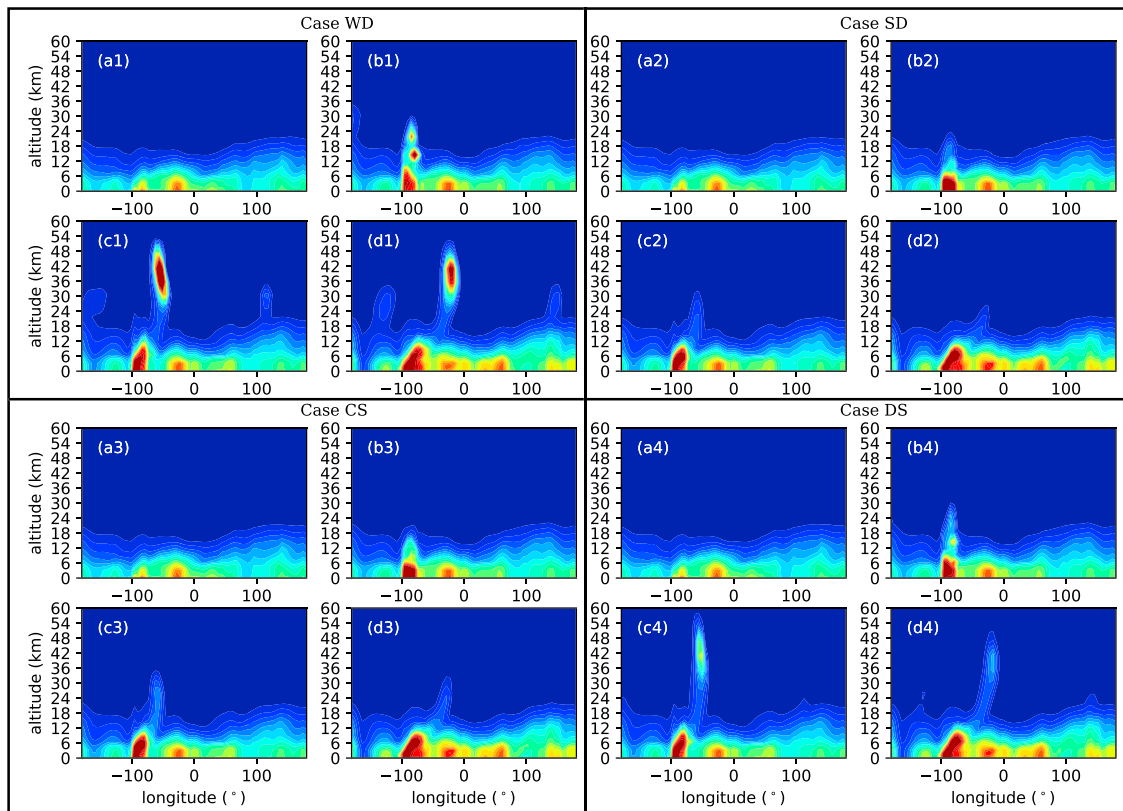
Figure 4. The cross sections of dust density-scaled opacity at the same time and location for comparison with the best-guess case in Figure 3 but from difference cases. The names of cases are labeled. The setting of parameters of different cases are listed in Table 1. The data are plotted with the same color bar in Figure 3. For each case, dust density-scaled opacity at local time 10:00, 15:00, 20:00, and 3:00 are shown.

4.2.3. Dust Injection Timing

The extra heating provides buoyancy for supporting the rocket dust storm's ascent/descent. During the daytime, it is obvious that the earlier the dust particles are injected, the longer they are exposed to sunlight; hence, the more solar energy they will absorb. As a result, the rocket dust storm can move upward for a longer time. When the start time of dust injection is moved 2 hr earlier to LT 08:00 (case EI) but retaining the same total dust injection period of 2 hr, dust particles are transported to ~42 km by LT 20:00 (Figure 5c5). This results in a higher detached dust layer than that in the best-guess case. Conversely, when the injection time is shifted 2 hr later (in case LI), this leads to less daytime exposure, hence less energy for vertical motion. As a result, the detached dust layer forms at ~20 km at LT 20:00 (Figure 5c6), lower than the one formed in the case BG.

Two simulations have been performed to test the sensitivity to the duration of dust lifting. For a given $\Delta\tau_{dust}$, the known amount of dust, estimated through equation (2), can be injected into the atmosphere over a longer (4 hr in case long injection [LoI]) or shorter (1 hr in case short injection [SI]) time period. Compared to the best-guess simulation, fewer dust particles are lifted in each GCM time step when the total injection period is longer. This leads to a less dusty air parcel. After the lifting, the difference in dust concentration between the rocket dust storm and the environment atmosphere is smaller than that in the best-guess case. Thus, following equation (5), less heating will be provided for supporting the ascent of the rocket dust storm. As shown in Figures 5a7–5d7, the rocket dust storm mainly remains below 30 km. In the SI case, by contrast, a far dustier storm is created and more absorption of solar energy is expected. For case SI, deeper convection is shown in Figures 5a8–5d8, and storm dust is transported up to ~40 km by LT 20:00.

5. Preliminary Comparison With MCS Observations
5.1. Simulation of a Deep Dust Event

In order to validate the performance of the new parameterization, the model simulations are compared with the MCS observations. To do this, an annual simulation of MY29 was run with the LMD Martian GCM with
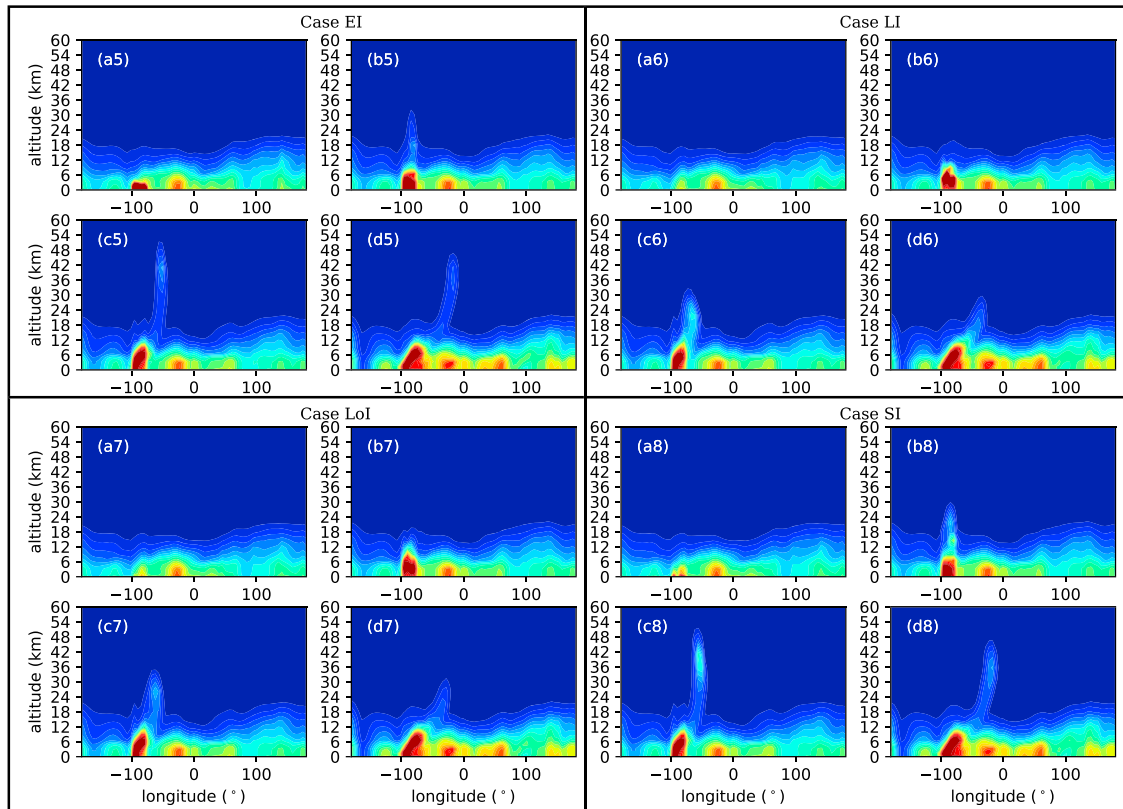
Figure 5. Same as Figure 4 except for cases EI, LI, LoI and SI.

and without the parameterization. For the purpose of comparison between model outputs and satellite observations, the nighttime MCS data are used due to their better spatial coverage and precision compared to the daytime MCS data and are compared to nighttime model output.

In MY29, around $L_s = 145°$, particularly opaque detached dust layers were observed by MCS in the Northern Hemisphere at latitudes around 30°N. The zonal mean dust DSO averaged from $L_s = 143°$ to 147° is shown in Figure 6a. These detached dust layers appeared suddenly and were considered to be generated by a deep dust event by analyzing consecutive L_s bins for the MCS nighttime zonal averaged dust DSO from $L_s = 130°$ to 165° (McCleese et al., 2010). After formation, the detached dust layers shifted equatorward and remained over the tropics after $L_s = 155°$. In the meantime, according to MARCI (the Mars Color Imager aboard MRO) observation report, a subregional dust storm occurred at $L_s =\sim 144.4°$ and lingered over Eastern Chryse and West Arabia (Malin et al., 2008). The spatiotemporal information of this dust storm hints strongly that it is the source of the MCS-observed detached dust layer at $L_s = 145°$.

In the MY29 prescribed dust scenario, the dust storm event observed by MARCI is included, as shown in Figures 6b and 6c. Figure 6c shows the global CDOD map at sol 310 of the MY29. A storm with an averaged dust optical depth larger than 2 is present. Figure 6b shows the temporal variation of dust optical depth at the center of the dust storm (indicated with a white star in Figure 6c). The dust optical depth in the center first increases by > 0.2 per sol in sol 307, which is sufficient to trigger the rocket dust storm process in the GCM. Consequently, this event provides a clear-cut example to assess the impact of this deep dust storm event on the dust structures in the GCM, with our new rocket dust storm parameterization. Since this dust event spread over several grid cells, it is simulated by triggering rocket dust storm parameterization in these grid cells as a collection of several individual rocket dust storms.

In Figure 7, the dust DSO distribution derived from the MCS observations is compared to simulations from the LMD Martian GCM with the rocket dust storm parameterization and from the traditional LMD Martian GCM (without the rocket dust storm parameterization). In Figures 7a, 7c, and 7e, the vertical variations in dust DSO
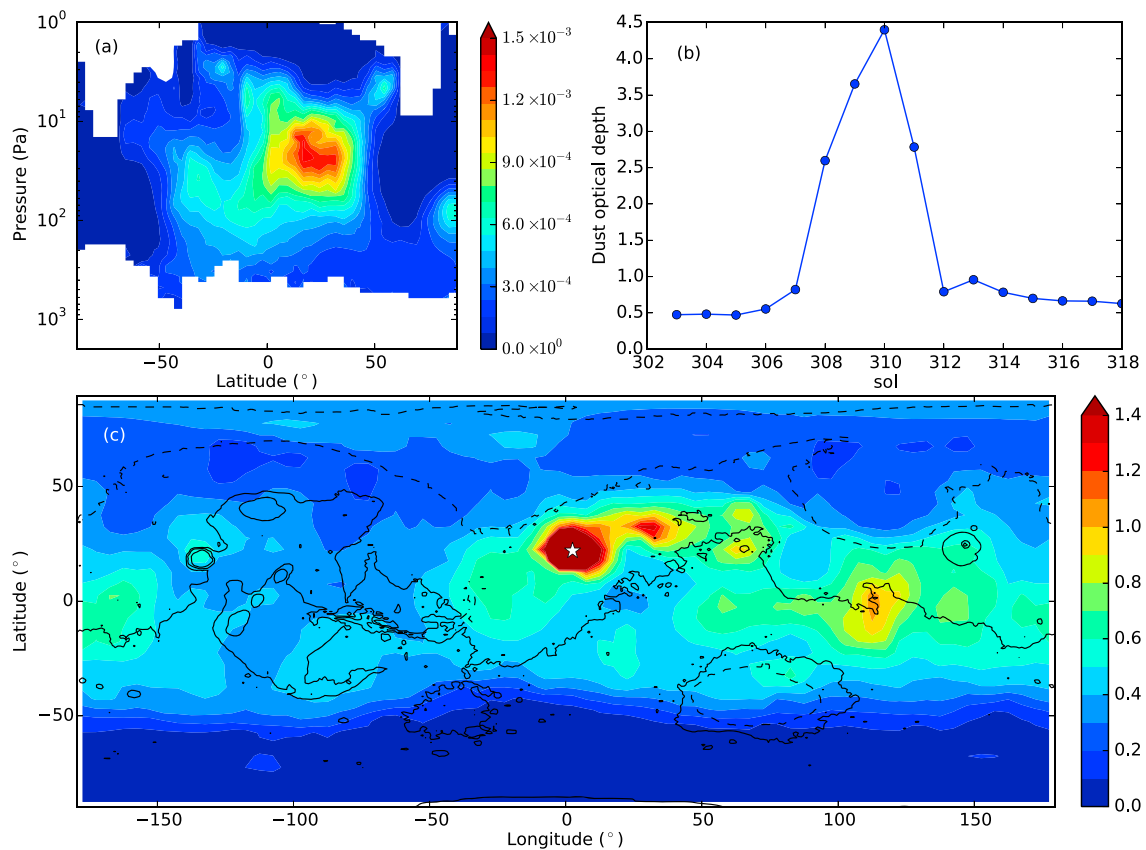
Figure 6. (a) The zonal mean of averaged Mars Climate Sounder-observed dust density-scaled opacity from $L_s = 143°$ to 147°. (b) The evolution of column dust optical depth at the location indicated with a white star in (c) the column dust optical depth map at $L_s = 146.0°$ in MY29.

from $L_s = 135°$ to 175° are shown, while in Figures 7b, 7d, and 7f, the dust DSO averaged over longitude and time (from $L_s = 145° - 150°$) are also displayed.

As can be seen in Figure 7a, before $L_s = 145°$, a thin detached dust layer is observed around 80 Pa. After $L_s = 145°$, the vertical dust distribution is significantly altered. The maximum of dust DSO is located at ~30 Pa (~30 km in altitude) and has been enriched by a factor of more than 2. Eventually, the detached dust layer moves downward and becomes fainter and fainter. Around $L_s = 170°$, the detached dust layer stops sedimenting at ~150 Pa. Note that the DSO near the surface is very low, about 5 times lower than the maximum of the DSO along the vertical. While in Figure 7c, the dust, simulated by the traditional LMD Martian GCM (without the rocket dust storm parameterization), is mostly concentrated near the surface.

In the simulation including the rocket dust storm parameterization (Figure 7e), the dust vertical distribution has been dramatically impacted compared to the results from the traditional Martian GCM (Figures 7c and 7d). Between $L_s \sim 140° - 150°$, a detached dust layer is formed, at an altitude similar to the MCS observation (Figures 7a and 7b). After the formation of this detached dust layer, the dust starts to sediment. The dust evolution in this detached layer from the MCS observation and the GCM with the rocket dust storm parameterization is comparable until $L_s \sim 160°$, although the simulated dust extends to slightly lower altitudes than the observed layer. In both cases, dust remains at a pressure level of ~100 Pa (~20 km). After that, a discrepancy in the dust vertical distribution becomes obvious. The dust observed by MCS tends to be stable at ~100 Pa, whereas the dust simulated by the model keep sedimenting down to the Martian surface.

In Figures 7b, 7d, and 7f, the dust DSO averaged over all longitudes and $L_s = 145° - 150°$ (which corresponds to the dustiest period in Figure 7a) are shown. The observations retrieved by MCS reveal that the detached dust layer in Figure 7a is located in the Northern Hemisphere, from the equator to ~40°N, whereas in Figure 7d, no detached dust layer can be identified above the PBL in the simulation using the traditional GCM. While in the simulation that includes the new parameterization (Figure 7f), a detached dust layer similar to that observed
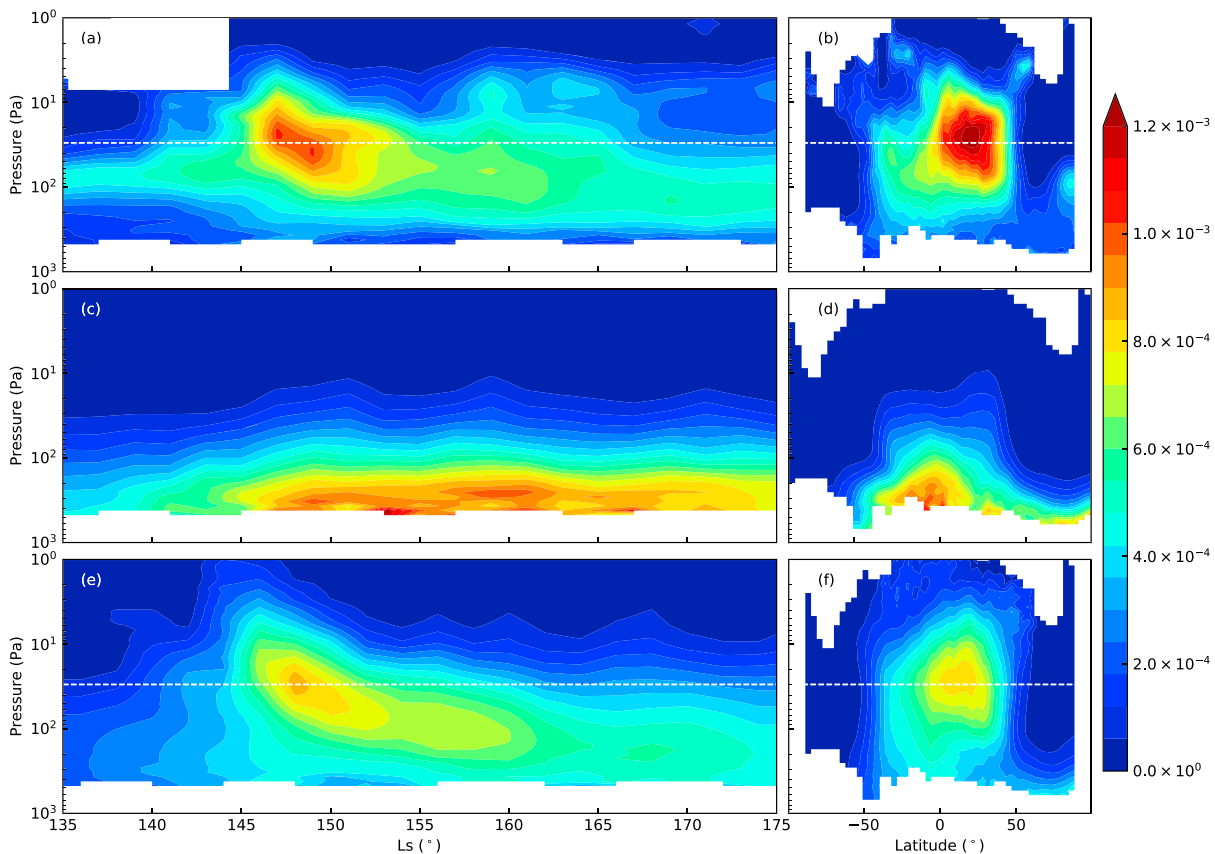
Figure 7. The nighttime dust density-scaled opacity (DSO) from the Mars Climate Sounder observation (a, b), compared to simulations by our traditional Global Climate Model (c, d) and by the Global Climate Model with the rocket dust storm parameterization (e, f). All data are binned in L_s (every 5°). In the left column, the dust DSO is averaged over latitude from 25°S to 25°N and all longitudes are plotted. In the right column, the zonal mean of dust DSO from $L_s = 145°$ to 150° are displayed. White dashed lines at a pressure of 30 Pa are plotted in the figure for better illustrating the altitude of the dust layers.

is produced. This dust layer is above the location where MARCI observed the reported dust storm (Malin et al., 2008). However, the GCM-derived peak DSO is lower than the MCS observation, that is, in Figures 7a and 7b. The fact that the model does not completely reproduce detached dust layers may suggest that not all dust layers are induced by dust storm events.

The reported deep dust event is also simulated by the LMD Martian GCM with the rocket dust storm parameterization but with different settings as described in Table 1. The simulated dust layers with the settings of cases WD, SD, CS, and DS are shown in Figure 8. In Figures 8a and 8b, a higher and dustier dust layer compared to the one in Figures 7e and 7f is produced with case WD setting. The dust concentration in this case is closer to the MCS observation (Figures 7a and 7b), but some extreme high dust layers are also simulated. A dust layer at a pressure of 1 Pa can be clearly seen in $L_s = 145°$. Another obvious dust layer at 5 Pa around $L_s = 140°$ can be recognized. Note that these detached dust layers are plotted with nighttime data. During the daytime, the GCM-simulated dust layers around L_s 140° and 145° are even higher than 5 and 1 Pa. Detached dust layers at these altitudes are not seen in the MCS observations. Therefore, a very weak detrainment is not recommended for the rocket dust storm parameterization. For the dust layer simulated with case SD setting, it is clearer and lower than the one shown in Figures 7e and 7f. Figures 8e–8h show the simulated dust layers with settings of different reference dust mass mixing ratios (cases CS and DS). The altitude and concentration of the dust layer in Figures 8e and 8f (case CS) are slightly lower than the one in Figures 7e and 7f (case BG). The layer simulated with dusty storm setting (case DS), however, is similar to the one simulated with best-guess setting. This may be attributed to the fact that this deep dust storm is so opaque that increasing its dustiness will not impact its energy balance significantly.

In Figure 9, the deep dust event is simulated with the settings of cases EI, LI, LoI, and SI. In the simulation in which dust is lifted over a long time period (case LoI), the DSO maximum peaks at a slightly lower altitude
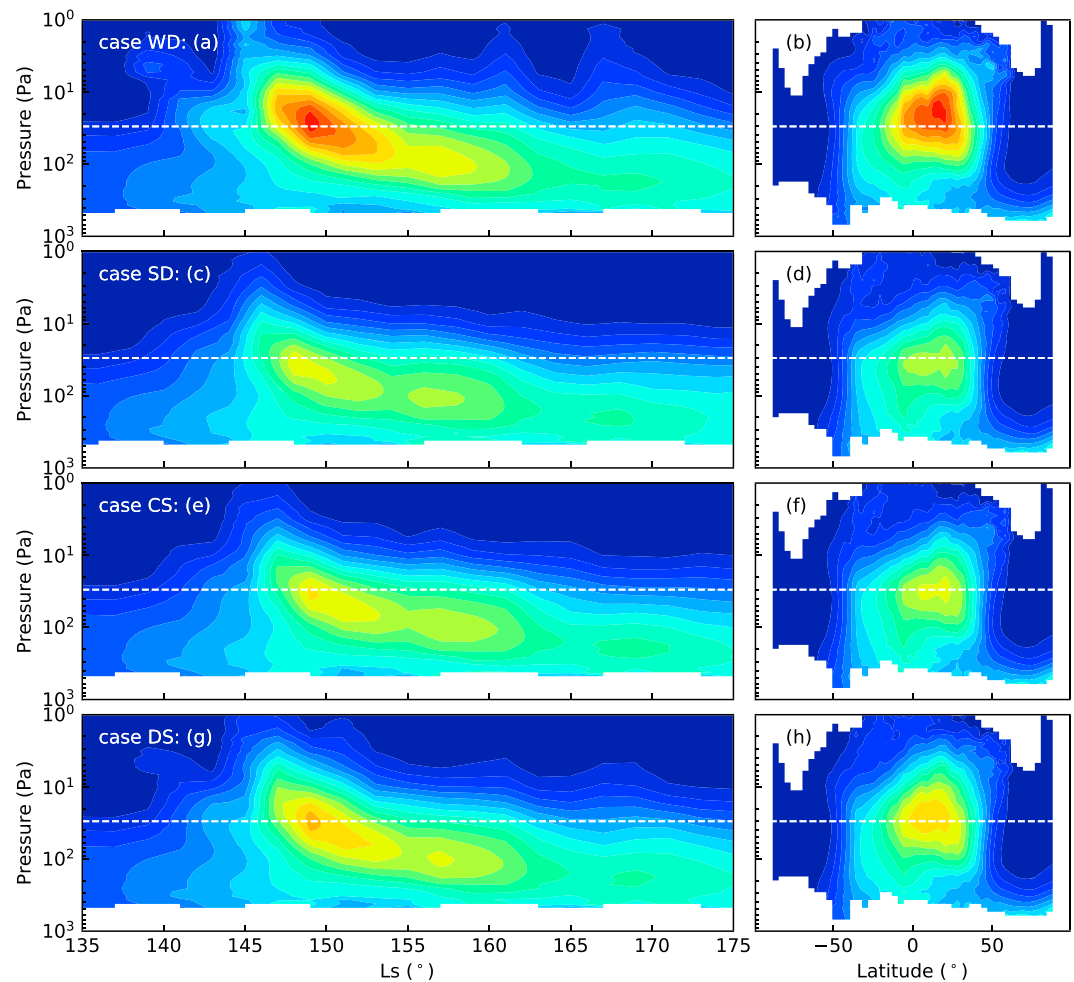
Figure 8. The nighttime dust density-scaled opacity analogous to Figure 7 simulated by the Global Climate Model with rocket dust storm parameterization but with the settings of cases (a, b) weak detrainment (WD), (c, d) strong detrainment (SD), (e, f) clear storm (CS), and (g, h) dusty storm (DS). The color bar is not shown since it is the same as the one used in Figure 7.

at $L_s \sim 149°$ compared to the one simulated with the best-guess setting. By contrast, at the same L_s, the DSO maximum in Figures 9g and 9h (case SI) appears at a slightly higher altitude than the one in Figures 7e and 7f. Although the differences of the altitudes where the dust layers in cases BG, LoI, and SI reached are subtle, the time period length of dust injection in these simulations has a similar impact on simulating the altitude of the detached dust layers as in the sensitivity experiments in section 4.2.3. In the sensitivity experiments, it is showed that earlier dust injection (case EI) results in a higher detached dust layer (see section 4.2.3), while when simulated, the deep dust event with case EI setting, a detached dust layer (Figures 9a and 9b) with comparable altitude to the one in Figures 7e and 7f (with case BG setting) is shown around $L_s = 150°$. This may be due to the fact that earlier dust injection results in a longer stay for dust above the PBL, thus storm dust interacts with environment dust for a longer time. Meanwhile, the dust may also travel along with the horizontal jets. These will lead to the dilution of the storm dust. This may be the reason why the DSO of the layers simulated with case EI setting (Figures 9a and 9b) is lower than those in Figures 7e and 7f. As a consequence, the low-concentration storm dust results in less absorption of the solar energy. This plays a contrary role to long time exposure of dust in the daytime which imply more absorption of solar energy. In fact, in the sensitivity experiments in section 4.2.3, the altitude of the detached dust layer formed in case EI in the sol after the rocket dust storm occurred (Figures 5a5–5d5) is not higher than the one formed in case BG (not shown in section 4; see their evolutions in the supporting information). In Figures 9c and 9d, the detached structures of the deep dust event with late dust injection (case LI) are shown. A lower detached dust layer is produced because less solar energy is absorbed.
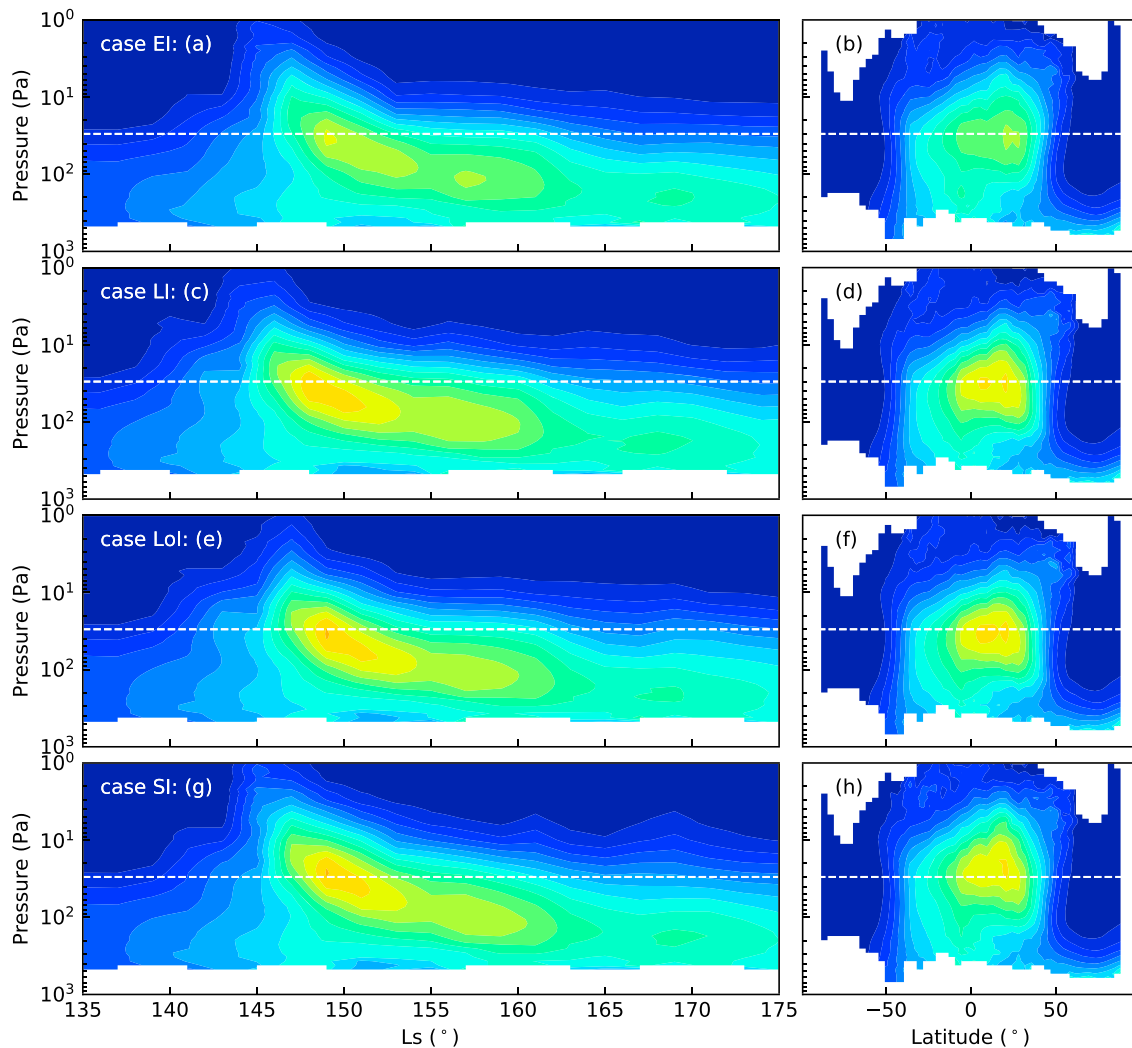
Figure 9. Same as Figure 8, but with the settings of cases early injection (EI), late injection (LI), long injection (LoI), and short injection (SI).

By simulating the reported deep dust event with a different set of parameters, the comparison as shown in Figures 8 and 9 reveals similar results in sensitivity studies, where an individual rocket dust storm is simulated. The detrainment of storm dust to environment dust impacts the formation of detached layers significantly. Meanwhile, varying dust contrast inside and outside of the storm and the time period over which the storm absorbs solar energy can change the supply of convective energy, which will subsequently have an effect on the production of the detached dust layers.

5.2. Annual Simulation Comparison

In Figure 10, the annual nighttime dust DSO vertical distribution over tropical regions during MY29 from the observations and from the GCM simulations (with and without the rocket dust storm parameterization) are shown. During the dusty seasons, the altitudes of the observed detached dust layers vary dramatically (Figure 10a), from 100 to 10 Pa ($\sim$38 km). Compared to the observations (Figure 10a), the detached dust layers produced in the GCM (with the rocket dust storm parameterization, Figure 10b) are comparable to the MCS-observed high-altitude detached layers. This implies that the vertical variation of the altitude of detached dust layers on Mars during the dusty season mostly originates from the deep dust storm events. However, the model simulation with the rocket dust storm process fails to account for the annual variations of the detached dust layers retrieved from the satellite observations, in particular, during the clear season. In Figure 10a, MCS data show that detached dust layers exist throughout the whole year. In the clear season, the detached dust layers' levels are quite stable at around 100 Pa, whereas these features of the detached dust layers are not reproduced by the GCM including the rocket dust storm parameterization. In the late summer (around L_s 120°),
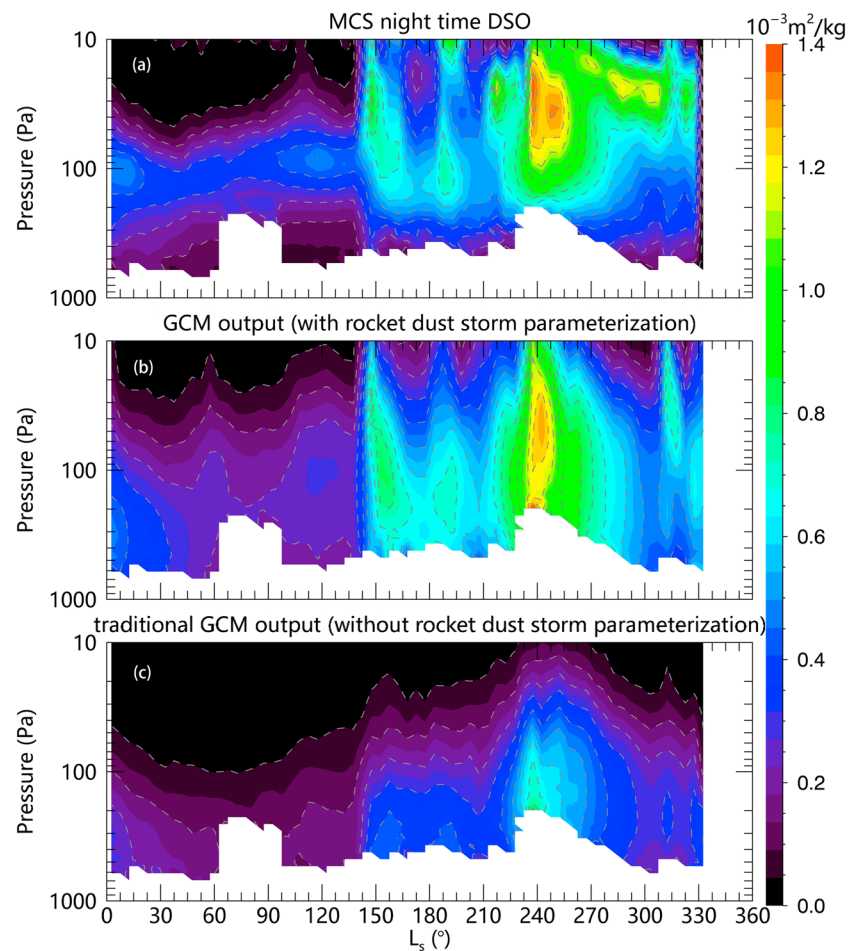
Figure 10. The temporal-vertical distribution of nighttime (local time 3:00) dust density-scaled opacity over tropical regions (averaged over all longitudes and 10°N to 10°S) at an infrared wavelength (21.6 μm) in MY29 from (a) Mars Climate Sounder observations, Global Climate Model output (b) with and (c) without the rocket dust storm parameterization.

the GCM produces detached dust layers, but the dust concentrations of these layers are lower than those in the MCS observations (Figure 10a). Meanwhile, no detached dust layers are produced at the beginning of the Martian year. The reason for these failures may be that, in the GCM, during the clear seasons, the dust scenario does not report significant variations of dust optical depth. This leads to fewer local dust storm onsets in this season. As a consequence, no obvious detached dust layers form ($L_s < 150°$ in Figure 10b). This may hint that the observed detached dust layers in the clear seasons may be formed by processes other than rocket dust storms. Meanwhile, the detached dust layers after $L_s \sim 270°$ in Figure 10a also cannot be explained by the rocket dust storms. These detached layers formed when fewer dust storms were reported (from MY29 dust scenario; dust activity starts to decrease after $L_s \sim 240°$; see Figure 21 in Montabone et al., 2015). In addition, the altitudes of these dust layers are even higher than those layers simulated around $L_s \sim 240°$, the dustiest time during MY29.

Another discrepancy between the simulation and the satellite observations is that, even if the rocket dust storms advect dust particles to high altitudes, the dust particles in the detached layers ultimately sediment onto the surface (similar to the dust distribution after $L_s > 160°$ in Figure 7e), resulting in the dissipation of the detached dust layers instead of remaining at an altitude of ~20 km as seen by MCS.

These two inconsistencies may imply that the detached dust layers may also be generated by some other atmospheric processes, such as slope winds and/or scavenging of dust particles by water ice as discussed in section 1. A mesoscale diurnal slope circulation may be capable of providing continuous upward convection

during the daytime, recycling dust particles into the atmosphere (Rafkin et al., 2002). Navarro, Madeleine, et al. (2014) report that in their GCM simulations, scavenging cannot explain the formation of detached dust layers because insufficient dust particles exist at the level where the water ice clouds are present. Another possibility for the inconsistencies between the model simulation and the observation could come from the missing observation of local rocket dust storms in the dust forcing scenarios. These dust scenarios are built based on the observations made by different Mars orbiting instruments. But if the rocket dust storm decays before or forms after the orbiter's operating local time, the instrument will be incapable of reporting the variation of dust concentration. The lack of rocket dust storms may be due to the imprecise set of the trigger criterion in this parameterization (see text in section 3.1), such as using a location or season varying $\Delta \tau_{\text{dust}}$ that could improve the onsets of dust storms. Besides, the inconsistencies may be attributed to the solar escalator mechanism, which plays a role in countering the dust sedimentation (Daerden et al., 2015). Dust motion analogous to the solar escalator can be seen in our simulations (not shown in this paper), but it is not strong enough to support the long-term sustenance of the detached dust layers, which can be verified by the fact that in Figures 7–9, all the GCM-simulated detached dust layers are sediment down to the surface. This may be due to the poor representation of the solar escalator (possibly because of the coarse GCM resolution), or it may imply that the solar escalator is not the key factor to sustain the detached dust layers. Moreover, the performance of the parameterization may be limited by its own ad hoc assumptions, such as the dust lifting scheme, the timing for dust injection, and/or the reference mass mixing ratio for estimating the dust storm's scale. Further observations of mesoscale dust motion may be helpful to implement more realistic versions of this parameterization.

6. Conclusion

In this paper, a rocket dust storm parameterization which is based on a parameterization of the dust transport by deep mesoscale convection during rocket dust storms, using global dust scenarios as a quantitative means to evaluate the occurrence of rocket dust storms, has been proposed and implemented in the LMD Martian GCM. This implementation allows dust to be efficiently advected to high altitudes in the atmosphere. This was not possible in large-scale traditional Martian GCMs. Model simulations show that the dust cycle in the GCM including this parameterization can produce detached dust layers similar to the observed ones when intense storms are simulated. This suggests that the rocket dust storms are a key phenomenon to account for the detached dust layers on Mars. Nevertheless, there are inconsistencies between the simulation and observations. Further model developments, regarding the impact of local topographic circulations, and/or dust-water ice interactions, are needed to fully explore the origins of the detached dust layers on Mars. Meanwhile, more observations concerning local dust storms may be helpful to refine this parameterization, such as how the trigger of dust storm and dust lifting vary with local meteorological conditions rather than with the dust scenarios in this study. Even though the vertical velocities of the rocket dust storms are comparable to mesoscale simulations, studies with respect to dust mixing are still needed to detail the behavior of mesoscale dust convection. In addition, other strategies for parameterizing rocket dust storms in GCMs are also possible and might be proposed in future work, echoing the diversity of cumulus parameterizations in terrestrial GCMs.

References

Basu, S., Richardson, M. I., & Wilson, R. J. (2004). Simulation of the Martian dust cycle with the GFDL Mars GCM. *Journal of Geophysical Research*, *109*, E11006. https://doi.org/10.1029/2004JE002243

Basu, S., Wilson, J., Richardson, M., & Ingersoll, A. (2006). Simulation of spontaneous and variable global dust storms with the GFDL Mars GCM. *Journal of Geophysical Research*, *111*, E09004. https://doi.org/10.1029/2005JE002660

Böing, S. J., Siebesma, A. P., Korpershoek, J. D., & Jonker, H. J. J. (2012). Detrainment in deep convection. *Geophysical Research Letters*, *39*, L21806. https://doi.org/10.1029/2012GL053735

Cantor, B. A. (2007). MOC observations of the 2001 Mars planet-encircling dust storm. *Icarus*, *186*, 60–96. https://doi.org/10.1016/j.icarus.2006.08.019

Cantor, B. A., James, P. B., Caplinger, M., & Wolff, M. J. (2001). Martian dust storms: 1999 Mars Orbiter Camera observations. *Journal of Geophysical Research*, *106*, 23,653–23,688. https://doi.org/10.1029/2000JE001310

Cantor, B. A., Kanak, K. M., & Edgett, K. S. (2006). Mars Orbiter Camera observations of Martian dust devils and their tracks (September 1997 to January 2006) and evaluation of theoretical vortex models. *Journal of Geophysical Research*, *111*, E12002. https://doi.org/10.1029/2006JE002700

Colaïtis, A., Spiga, A., Hourdin, F., Rio, C., Forget, F., & Millour, E. (2013). A thermal plume model for the Martian convective boundary layer. *Journal of Geophysical Research: Planets*, *118*, 1468–1487. https://doi.org/10.1002/jgre.20104

Conrath, B. J. (1975). Thermal structure of the Martian atmosphere during the dissipation of dust storm of 1971. *Icarus*, *24*, 36–46. https://doi.org/10.1016/0019-1035(75)90156-6

Daerden, F., Whiteway, J. A., Neary, L., Komguem, L., Lemmon, M. T., Heavens, N. G., et al. (2015). A solar escalator on Mars: Self-lifting of dust layers by radiative heating. *Geophysical Research Letters*, *42*, 7319–7326. https://doi.org/10.1002/2015GL064892

de Rooy, W. C., Bechtold, P., Fröhlich, K., Hohenegger, C., Jonker, H., Mironov, D., et al. (2013). Entrainment and detrainment in cumulus convection: An overview. *Quarterly Journal of the Royal Meteorological Society*, *139*(670), 1–19. https://doi.org/10.1002/qj.1959

de Rooy, W. C., & Siebesma, A. (2010). Analytical expressions for entrainment and detrainment in cumulus convection. *Quarterly Journal of the Royal Meteorological Society*, *136*(650), 1216–1227. https://doi.org/10.1002/qj.640

Fisher, J. A., Richardson, M. I., Newman, C. E., Szwast, M. A., Graf, C., Basu, S., et al. (2005). A survey of Martian dust devil activity using Mars Global Surveyor Mars Orbiter Camera images. *Journal of Geophysical Research*, *110*, E03004. https://doi.org/10.1029/2003JE002165

Forget, F., Hourdin, F., Fournier, R., Hourdin, C., Talagrand, O., Collins, M., et al. (1999). Improved general circulation models of the Martian atmosphere from the surface to above 80 km. *Journal of Geophysical Research*, *104*, 24,155–24,175. https://doi.org/10.1029/1999JE001025

Forget, F., Millour, E., Madeleine, J.-B., Colaitis, A., Spiga, A., Montabone, L., et al. (2011). Back to the basics: Improving the prediction of temperature, pressure and winds in the LMD general circulation model. In F. Forget & E. Millour (Eds.), *Mars Atmosphere: Modelling and Observation* (pp. 64–67). Paris, France: Scientific Committee.

Guzewich, S. D., Talaat, E. R., Toigo, A. D., Waugh, D. W., & McConnochie, T. H. (2013). High-altitude dust layers on Mars: Observations with the Thermal Emission Spectrometer. *Journal of Geophysical Research: Planets*, *118*, 1177–1194. https://doi.org/10.1002/jgre.20076

Heavens, N. G., Benson, J. L., Kass, D. M., Kleinböhl, A., Abdou, W. A., McCleese, D. J., et al. (2010). Water ice clouds over the Martian tropics during northern summer. *Geophysical Research Letters*, *37*, L18202. https://doi.org/10.1029/2010GL044610

Heavens, N. G., Cantor, B. A., Hayne, P. O., Kass, D. M., Kleinböhl, A., McCleese, D. J., et al. (2015). Extreme detached dust layers near Martian volcanoes: Evidence for dust transport by mesoscale circulations forced by high topography. *Geophysical Research Letters*, *42*, 3730–3738. https://doi.org/10.1002/2015GL064004

Heavens, N. G., Johnson, M. S., Abdou, W. A., Kass, D. M., Kleinböhl, A., McCleese, D. J., et al. (2014). Seasonal and diurnal variability of detached dust layers in the tropical Martian atmosphere. *Journal of Geophysical Research: Planets*, *119*, 1748–1774. https://doi.org/10.1002/2014JE004619

Heavens, N. G., McCleese, D. J., Richardson, M. I., Kass, D. M., Kleinböhl, A., & Schofield, J. T. (2011). Structure and dynamics of the Martian lower and middle atmosphere as observed by the Mars Climate Sounder: 2. Implications of the thermal structure and aerosol distributions for the mean meridional circulation. *Journal of Geophysical Research*, *116*, E010101. https://doi.org/10.1029/2010JE003713

Heavens, N. G., Richardson, M. I., Kleinböhl, A., Kass, D. M., McCleese, D. J., Abdou, W., et al. (2011a). Vertical distribution of dust in the Martian atmosphere during northern spring and summer: High-altitude tropical dust maximum at northern summer solstice. *Journal of Geophysical Research*, *116*, E01007. https://doi.org/10.1029/2010JE003692

Heavens, N. G., Richardson, M. I., Kleinböhl, A., Kass, D. M., McCleese, D. J., Abdou, W., et al. (2011b). The vertical distribution of dust in the Martian atmosphere during northern spring and summer: Observations by the Mars Climate Sounder and analysis of zonal average vertical dust profiles. *Journal of Geophysical Research*, *116*, E04003. https://doi.org/10.1029/2010JE003691

Hourdin, F. (1992). A new representation of the CO_2 15 μm band for a Martian general circulation model. *Journal of Geophysical Research*, *97*(E11), 18,319–18,335.

Hourdin, F., & Armengaud, A. (1999). Test of a hierarchy of finite-volume schemes for transport of trace species in an atmospheric general circulation model. *Monthly Weather Review*, *127*, 822–837.

Kahre, M. A., Murphy, J. R., & Haberle, R. M. (2006). Modeling the Martian dust cycle and surface dust reservoirs with the NASA Ames general circulation model. *Journal of Geophysical Research*, *111*, E06008. https://doi.org/10.1029/2005JE002588

Määttänen, A., Fouchet, T., Forni, O., Melchiorri, R., Forget, F., Savijarvi, H., et al. (2009). A study of the properties of a local dust storm with Mars Express OMEGA and PFS data. *Icarus*, *201*(2), 504–516. https://doi.org/10.1016/j.icarus.2009.01.024

Määttänen, A., Listowski, C., Montmessin, F., Maltagliati, L., Reberac, A., Joly, L., & Bertaux, J.-L. (2013). A complete climatology of the aerosol vertical distribution on Mars from MEx/SPICAM UV solar occultations. *Icarus*, *223*, 892–941. https://doi.org/10.1016/j.icarus.2012.12.001

Madeleine, J.-B., Forget, F., Millour, E., Montabone, L., & Wolff, M. J. (2011). Revisiting the radiative impact of dust on Mars using the LMD Global Climate Model. *Journal of Geophysical Research*, *116*, E11010. https://doi.org/10.1029/2011JE003855

Madeleine, J.-B., Forget, F., Millour, E., Navarro, T., & Spiga, A. (2012). The influence of radiatively active water ice clouds on the Martian climate. *Geophysical Research Letters*, *39*, L23202. https://doi.org/10.1029/2012GL053564

Malin, M. C., Cantor, B. A., Kennedy, M. R., Shean, D. E., & Harrison, T. N. (2008). MRO MARCI weather report for the week of 20 October 2008-26 October 2008. *Malin Space Science Systems Captioned Image Release, MSSS-56*.

McCleese, D. J., Heavens, N. G., Schofield, J. T., Abdou, W. A., Bandfield, J. L., Calcutt, S. B., et al. (2010). Structure and dynamics of the Martian lower and middle atmosphere as observed by the Mars Climate Sounder: Seasonal variations in zonal mean temperature, dust, and water ice aerosols. *Journal of Geophysical Research*, *115*, E12016. https://doi.org/10.1029/2010JE003677

McCleese, D. J., Schofield, J. T., Taylor, F. W., Calcutt, S. B., Foote, M. C., Kass, D. M., et al. (2007). Mars Climate Sounder: An investigation of thermal and water vapor structure, dust and condensate distributions in the atmosphere, and energy balance of the polar regions. *Journal of Geophysical Research*, *112*, E05S06. https://doi.org/10.1029/2006JE002790

Montabone, L., Forget, F., Millour, E., Wilson, R., Lewis, S., Cantor, B., et al. (2015). Eight-year climatology of dust optical depth on Mars. *Icarus*, *251*, 65–95. https://doi.org/10.1016/j.icarus.2014.12.034

Montmessin, F., Forget, F., Rannou, P., Cabane, M., & Haberle, R. M. (2004). Origin and role of water ice clouds in the Martian water cycle as inferred from a general circulation model. *Journal of Geophysical Research*, *109*, E10004. https://doi.org/10.1029/2004JE002284

Mulholland, D. P., Read, P. L., & Lewis, S. R. (2013). Simulating the interannual variability of major dust storms on Mars using variable lifting thresholds. *Icarus*, *223*, 344–358. https://doi.org/10.1016/j.icarus.2012.12.003

Mulholland, D. P., Spiga, A., Listowski, C., & Read, P. L. (2015). An assessment of the impact of local processes on dust lifting in Martian climate models. *Icarus*, *252*, 212–227. https://doi.org/10.1016/j.icarus.2015.01.017

Navarro, T., Forget, F., Millour, E., & Greybush, S. J. (2014). Detection of detached dust layers in the Martian atmosphere from their thermal signature using assimilation. *Geophysical Research Letters*, *41*, 6620–6626. https://doi.org/10.1002/2014GL061377

Navarro, T., Madeleine, J.-B., Forget, F., Spiga, A., Millour, E., & Montmessin, F. (2014). Global Climate Modeling of the Martian water cycle with improved microphysics and radiatively active water ice clouds. *Journal of Geophysical Research: Planets*, *119*, 1479–1495. https://doi.org/10.1002/2013JE004550

Newman, C. E., & Richardson, M. I. (2015). The impact of surface dust source exhaustion on the Martian dust cycle, dust storms and interannual variability, as simulated by the MarsWRF general circulation model. *Icarus*, *257*, 47–87. https://doi.org/10.1016/j.icarus.2015.03.030

Newman, C. E., Lewis, S. R., Read, P. L., & Forget, F. (2002). Modeling the Martian dust cycle 2. Multiannual radiatively active dust transport simulations. *Journal of Geophysical Research*, *107*(E12), 5124. https://doi.org/10.1029/2002JE001920

Rafkin, S. C. R. (2009). A positive radiative-dynamic feedback mechanism for the maintenance and growth of Martian dust storms. *Journal of Geophysical Research*, *114*, E01009. https://doi.org/10.1029/2008JE003217

Rafkin, S. C. R. (2012). The potential importance of non-local, deep transport on the energetics, momentum, chemistry, and aerosol distributions in the atmospheres of Earth, Mars, and Titan. *Planetary and Space Science*, *60*, 147–154. https://doi.org/10.1016/j.pss.2011.07.015

Rafkin, S. C. R., Sta Maria, M. R. V., & Michaels, T. I. (2002). Simulation of the atmospheric thermal circulation of a Martian volcano using a mesoscale numerical model. *Nature*, *419*, 697–699.

Smith, M. D., Wolff, M. J., Clancy, R. T., Kleinböhl, A., & Murchie, S. L. (2013). Vertical distribution of dust and water ice aerosols from CRISM limb-geometry observations. *Journal of Geophysical Research: Planets*, *118*, 321–334. https://doi.org/10.1002/jgre.20047

Spiga, A. (2011). Elements of comparison between Martian and terrestrial mesoscale meteorological phenomena: Katabatic winds and boundary layer convection. *Planetary and Space Science*, *59*, 915–922. https://doi.org/10.1016/j. pss.2010.04.025

Spiga, A., Faure, J., Madeleine, J.-B., Määttänen, A., & Forget, F. (2013). Rocket dust storms and detached dust layers in the Martian atmosphere. *Journal of Geophysical Research: Planets*, *118*, 746–767. https://doi.org/10.1002/jgre.20046

Van Leer, B. (1977). Towards the ultimate conservative difference scheme: IV. A new approach to numerical convection. *Journal of Computational Physics*, *23*, 276–299.

Wang, H., & Richardson, M. I. (2015). The origin, evolution, and trajectory of large dust storms on Mars during Mars years 24-30 (1999-2011). *Icarus*, *251*, 112–127. https://doi.org/10.1016/j.icarus.2013.10.033

Wolff, M. J., Smith, M. D., Clancy, R. T., Arvidson, R., Kahre, M., Seelos, F., et al. (2009). Wavelength dependence of dust aerosol single scattering albedo as observed by the Compact Reconnaissance Imaging Spectrometer. *Journal of Geophysical Research*, *114*, E00D04. https://doi.org/10.1029/2009JE003350

Wolff, M. J., Smith, M. D., Clancy, R. T., Spanovich, N., Whitney, B. A., Lemmon, M. T., et al. (2006). Constraints on dust aerosols from the Mars Exploration Rovers using MGS overflights and Mini-TES. *Journal of Geophysical Research*, *111*, E12S17. https://doi.org/10.1029/2006JE002786

Ye, Z. J., Segal, M., & Pielke, R. A. (1990). A comparative study of daytime thermally induced upslope flow on Mars and Earth. *Journal of the Atmospheric Sciences*, *47*, 612–628.